Article

Synthesis of Ilmenite Nickel Titanite-Supported Carbon Nanofibers Derived from Polyvinylpyrrolidone as Photocatalyst for H_2 Production from Ammonia Borane Photohydrolysis

Ibrahim M. Maafa [1],*, Nasser Zouli [1], Ahmed Abutaleb [1], Ayman Yousef [1,2],*, Isam Y. Qudsieh [1], Saleh M. Matar [1,3], Abdel Samed M. Adam [1] and M. M. El-Halwany [4]

[1] Department of Chemical Engineering, College of Engineering, Jazan University, Jazan 45142, Saudi Arabia; nizouli@jazanu.edu.sa (N.Z.); azabutaleb@jazanu.edu.sa (A.A.); isamyq@jazanu.edu.sa (I.Y.Q.); salehmatar@yahoo.com (S.M.M.); aabaker@jazanu.edu.sa (A.S.M.A.)

[2] Department of Mathematics and Physics Engineering, College of Engineering at Mataria, Helwan University, Cairo 11718, Egypt

[3] Bioprocess Development Department, Genetic Engineering and Biotechnology Research Institute (GEBRI), City of Scientific Research and Technological Applications (SRTA-City), New Borg El-Arab City, Alexandria 21934, Egypt

[4] Department of Mathematics and Physics Engineering, College of Engineering, Mansoura University, El-Mansoura 35516, Egypt; mmelhalwany@yahoo.com

* Correspondence: imoaafa@jazanu.edu.sa (I.M.M.); aymanyousef84@gmail.com (A.Y.)

Abstract: The present study involves the synthesis of photocatalytic composite nanofibers (NFs) comprising ilmenite nickel titanite-supported carbon nanofibers ($NiTiO_3/TiO_2$@CNFs) using an electrospinning process. The photocatalytic composite NFs obtained were utilized in hydrogen (H_2) production from the photohydrolysis of ammonia borane (AB). The experimental findings show that the photocatalytic composite NFs with a loading of 25 mg had a good catalytic performance for H_2 generation, producing the stoichiometric H_2 in 11 min using 1 mmol AB under visible light at 25 °C and 1000 rpm. The increase in catalyst load to 50, 75, and 100 mg leads to a corresponding reduction in the reaction time to 7, 5, and 4 min. The findings from the kinetics investigations suggest that the rate of the photohydrolysis reaction is directly proportional to the amount of catalyst in the reaction system, adhering to a first-order reaction rate. Furthermore, it was observed that the reaction rate remains unaffected by the concentration of AB, thereby suggesting a reaction of zero order. Increasing the reaction temperature results in a decrease in the duration of the photohydrolysis reaction. Furthermore, an estimated activation energy value of 35.19 kJ mol^{-1} was obtained. The composite nanofibers demonstrated remarkable and consistent effectiveness throughout five consecutive cycles. The results suggest that composite NFs possess the capacity to function as a feasible substitute for costly catalysts in the process of H_2 generation from AB.

Keywords: ilmenite; ammonia borane; polyvinylpyrrolidone; hydrogen; electrospinning; photohydrolysis

1. Introduction

Hydrogen (H_2) energy is an environment-friendly source of energy that is gaining interest across the globe because of its potential to alleviate the energy crisis, facilitate the transformation of the energy sector, and mitigate the effects of climate change and pollution [1–3]. The use of a H_2 economy in our day-to-day lives is still meeting a great number of challenges, the foremost of which is the storage of H_2 [4,5]. A possibility is to store H_2 in the form of solid-state H_2 storage, which relies on either physical or chemical interactions between H_2 and storage materials [6,7]. Among these, amine-borane stands out as an effective hydrogen storage material because it satisfies a number of requirements set by the United States Department of Energy (DOE): (a) possessing a significant amount

of hydrogen, (b) stability, and (c) eco-friendliness [8,9]. Ammonia borane (NH_3BH_3) is the most basic form of the amine-borane compounds that is being studied for its potential use in solid hydrogen storage material due to its high (19.6 wt.%) hydrogen content [10,11]. Hydrogen produced by the photocatalytic hydrolysis of AB with the help of light has attracted a lot of attention because it is a promising clean, efficient, and infinite energy source [11,12]. Ayman et al. published the first proof of AB photohydrolysis in 2012 [13]. Since then, several studies have been conducted to determine the efficacy of various photocatalytic substances in generating hydrogen from AB [14–16]. The photohydrolysis method can produce gravimetric hydrogen capacity in AB, which is comparable to what happens during normal hydrolysis; however, radiation from light could be able to restrict the generation of ammonia [17]. Various metal- and non-metal-supported TiO_2 have been used as efficient photocatalysts for the production of H_2 from the photohydrolysis of AB [14,17–22]. Over the last several years, ilmenite has been developed as an effective visible-light-driven photocatalyst [23–26]. Because of its adequate bandgap and capacity to absorb solar radiation, nickel titanate ($NiTiO_3$, Eg~2.18 eV) has been identified as a suitable photocatalytic material for various reactions [27]. Huang et al. [28] produced $NiTiO_3/TiO_2$ nanotubes and used them to produce H_2 by photosplitting. The fabricated $NiTiO_3/TiO_2$ showed promising photocatalytic performance with H_2 generation rates of 45 and 680 mol g^{-1} h^{-1} for TiO_2 and $NiTiO_3/TiO_2$, respectively. Carbon nanofibers (CNFs) have been demonstrated to possess excellent electrical conductivity, which means that they may readily gather and transfer photo-induced charges during the photocatalytic process [29]. In this investigation, we report for the first time on the production of $NiTiO_3/TiO_2@CNFs$ and their photocatalytic activity towards AB photohydrolysis. The catalyst is synthesized employing an electrospinning approach. The produced NFs exhibited excellent photocatalytic activity for H_2 generation via AB photohydrolysis.

2. Experimental

2.1. Preparation of Composite NFs

The sol–gel method was used to manufacture TiO_2-decorated CNFs. This was accomplished by combining 20 g of 12% solution of polyvinylpyrrolidone (PVP, 99.5%, Sigma Aldrich, USA) with 3 mL titanium isopropoxide (TIIP, 97%, Sigma Aldrich, USA). The PVP solution was prepared following the procedures described in other studies [30–35]. After stirring the mixture for an adequate duration of time, a translucent yellow gel is formed. In the laboratory-scale electrospinning apparatus, the formed sol–gel is introduced into the plastic syringe. The positive electrode is attached to the metallic tip of the plastic syringe, while the negative electrode is attached to a rotating metallic cylinder enclosed within wax foil. Throughout the spinning process, the potential and space between the positive and negative electrodes were kept as 20 kV and 15 cm, respectively. After the NF mats had formed on the foil, they were peeled off and dried in a vacuum drier overnight at 60 °C. The material was then calcined under vacuum in an Ar atmosphere at 950 °C for 5 h. Following the same protocol as before, nickel acetate tetrahydrate (NiAc, 98.5%, Sigma Aldrich, USA) was added and stirred. The same electrospinning and calcination methods were used once a translucent green solution was obtained.

2.2. Characterization

The synthesized composite was characterized using scanning electron microscopy, X-ray diffraction, and transmission electron microscopy. The details of these techniques have been discussed in our previous work [35].

2.3. Photohydrolysis of AB

The photocatalytic performance of the prepared NFs for H_2 production employing the photohydrolysis of AB was investigated. An LED (λ = 365 nm) light served as the source of illumination. A three-neck flask was used as the reactor. The water-displacement method was used to evaluate the volume of H_2 produced. After adding 1 mmol of ammonia borane

complex (AB, 97.0%) and 25 mg of catalyst to the reaction reactor, the charge was subjected to visible light to determine the produced H_2. In order to eliminate ammonia, the formed H_2 was passed through a 0.001 M HCl solution. There are several factors that have been studied, such as the concentration of AB, amount of catalyst, and reaction temperature.

3. Results and Discussion

Electrospun nanofibers (NFs) composed of TIIP-PVP, as shown in Figure 1a, are smooth and bead-free following sintering at 950 °C for 5 h in a vacuum in an Ar atmosphere. The FESEM image displayed in Figure 1b was acquired after the calcination of electrospun NFs composed of NiAc, TIIP, and PVP at 950 °C for five hours in a vacuum containing argon. As can be seen in Figure 1a, the NFs maintained their structure with the growth of very small NPs on the surface of the NFs. According to the results of the EDX study (Figure 1c), the NFs are mostly composed of nickel (Ni), titanium (Ti), oxygen (O), and carbon (C), and no additional elements have been found. FESEM-EDX images (Figure 1b,c) showed the formation of NPs on the surface of NFs. The EDX analysis demonstrated the presence of Ti, O, C, and Ni elements in the spectra. It is possible that the presence of carbon is making the photocatalytic process more efficient overall by doing the following: increasing the adsorption of AB molecules, which in turn increases the rate at which they are hydrolyzed by the photo-inducement of e− and h+ separation.
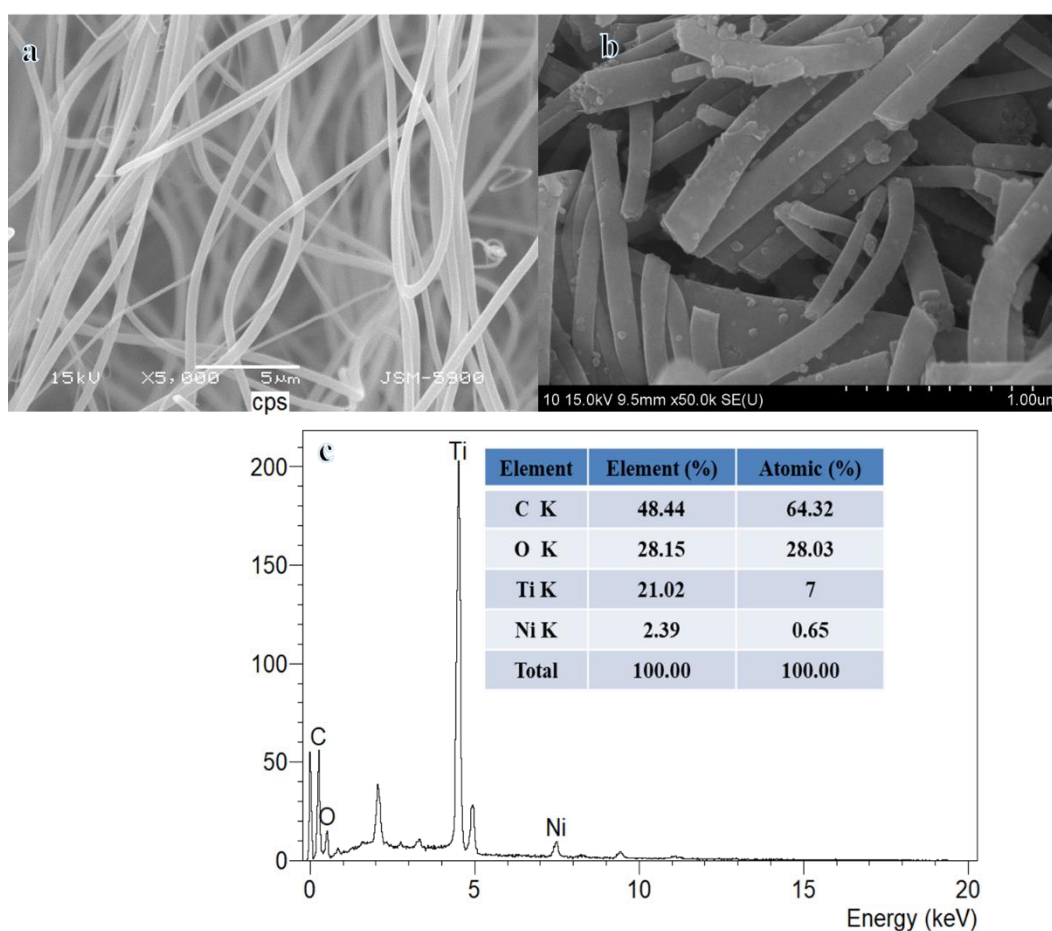

Element	Element (%)	Atomic (%)
C K	48.44	64.32
O K	28.15	28.03
Ti K	21.02	7
Ni K	2.39	0.65
Total	100.00	100.00

Figure 1. (**a**) SEM image of TIIP-PVP, (**b**) FESEM image, and (**c**) EDX analysis of composite NFs obtained after sintering at 950 °C in Ar.

The XRD data of the composite that was produced after the calcination procedure are shown in Figure 2. One peak of the TiO_2 phases, the rutile phase (JCPDS #00-004- 0551), was found to develop at a 2θ of 36.65°, matching the (101) crystal plane. Furthermore, a hexagonal $NiTiO_3$ phase of ilmenite (JCPDS #12035-39-1) occurred at 2θ of 42.32°, 62.09°,

and 74.47°, corresponding to the (021), (214), and (217) crystal orientations, respectively. The NPs' sizes were determined to be 8.43 nm using Scherrer's equation. Carbon-like graphite, which develops as a result of a partial degradation of carbon during the calcination process, has an outside peak at a 2θ that agrees with (002). The XRD of TiO$_2$@CNFs has been shown in our previous work [36].
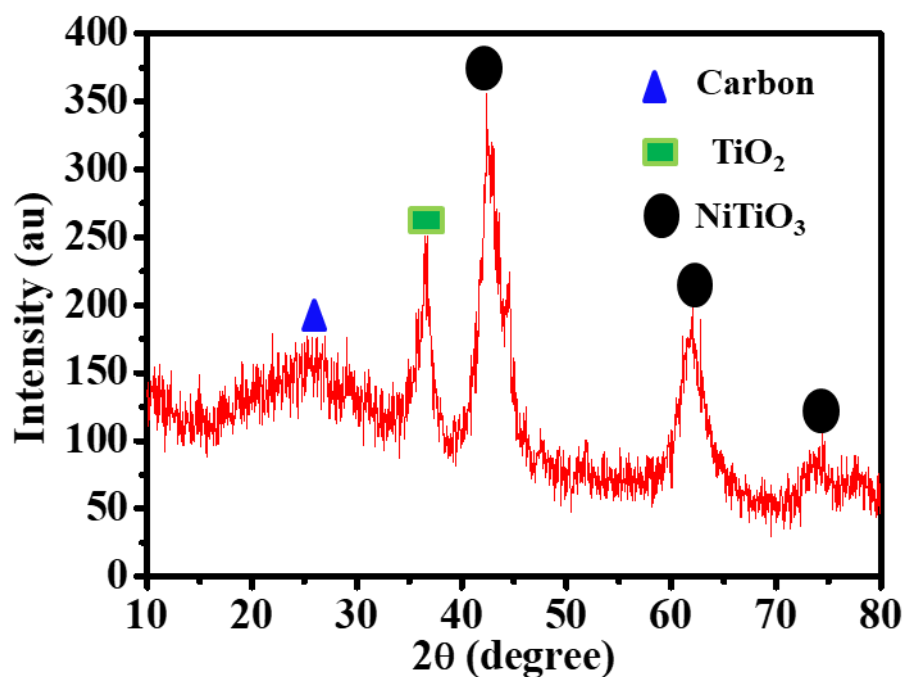

Figure 2. XRD analysis of composite NFs after sintering at 950 °C in Ar.

3.1. Photodehydrogenation of AB

It is interesting to mention that CNFs have been used as a supporting matrix in different reactions, but they did not exhibit any catalytic activity towards the dehydrogenation of AB, whereas a Ni-based catalyst demonstrated superior performance in both the catalytic and photocatalytic processes involved in H$_2$ production from AB [13,37,38]. This study evaluated the photodehydrogenation efficiency of pristine TiO$_2$ and composite NFs in the process of releasing hydrogen from the hydrolysis of AB (1 mmol AB) under visible illumination (λ = 365 nm) at a temperature of 25 °C and 1000 rpm (Figure 3). The total volume of H$_2$ produced with regard to pristine TiO$_2$ and composite NFs have been estimated to be 9 and 67 mL within a 12 min period, respectively. The activity of composite nanofibers was found to be significantly higher in comparison to pristine TiO$_2$.

The observed phenomenon may be attributed to the rapid separation of electron–hole pairs in composite nanofibers, which causes an increased number of ions in the solution, thereby enhancing hydrogen production via photodehydrogenation of AB in comparison to pristine TiO$_2$. The free radicals created in the solution upon exposure to sunlight could be the reason for this observation; these radicals assault the AB molecules in order to release hydrogen. The finding that the generation of H$_2$ was notably augmented when subjected to visible illumination in contrast to dark conditions is a topic of interest. In the absence of a catalyst, the stability of AB in water was evidenced by the absence of H$_2$ detection even under visible illumination.
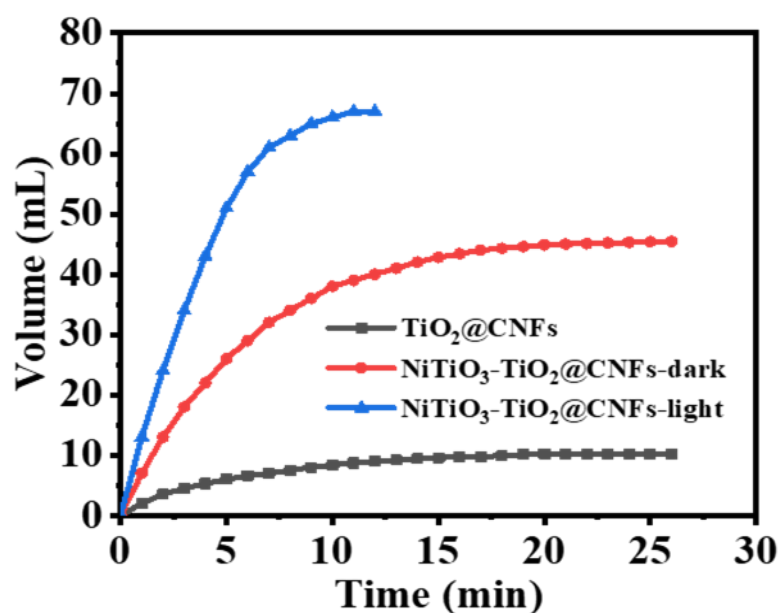
Figure 3. Volume of H_2 production from AB solution vs. time in the existence of photocatalysts under light irradiation (25 mg of photocatalyst, 25 °C, 1 mmol AB, and 1000 rpm).

3.2. Influence of Composite NF Loading

Figure 4a depicts the relationship between the equivalent produced H_2 and the duration of exposure to light at varying loads of composite NFs (25, 50, 75, and 100 mg). The results indicate that a rise in the load of composite NFs leads to a corresponding rise in the rate of H_2 generation. Furthermore, the four doses demonstrated activities with the following Turn Over Frequency (TOF) values: 12.84, 22.02, 25.69, and 38.53 $mol_{(H2)} \ mol_{(cat)}^{-1} \ min^{-1}$ for 25, 50, 75, and 100 mg of composite NFs, respectively. This phenomenon can be attributed to the enhanced surface area of the composite NFs, which enhances the photodehydrogenation of AB.

Figure 4b illustrates the natural logarithm of the reaction rate plotted against the natural logarithm of the composite NF load. The calculated slope of the optimal regression line is 0.87, indicating that the photodehydrogenation of H_2 conforms to the principles of pseudo-first-order kinetics with respect to the catalyst loading.
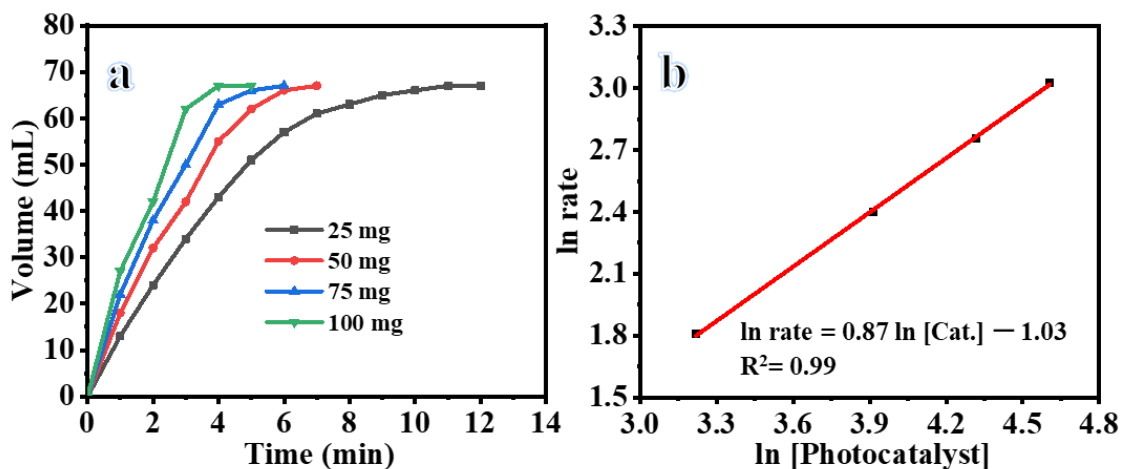

Figure 4. (**a**) Influence of photocotalyst on H_2 production, and (**b**) H_2 production rate vs. amount of photocatalyst on logarithmic scale (25 °C, 1 mmol AB, and 1000 rpm).

3.3. Influence of AB Concentration

The impact of varying initial AB concentrations (1, 2, 3, and 4 mmol) on the generation of H_2 through AB photodehydrogenation under visible illumination while utilizing composite NFs was investigated (Figure 5a). As illustrated in the graph, the concentration of AB did not have a significant impact on the rate of H_2 production. Specifically, the initial rate of H_2 generation remained relatively constant despite an increase in AB concentration. The utilization of varying AB concentrations in the photogeneration of H_2 can be attributed to a pseudo-zero-order reaction, as depicted in Figure 5b. The calculated slope of the regression line was 0.11, indicating that the hydrogen production rate adheres to pseudo-zero-order kinetics related to AB.
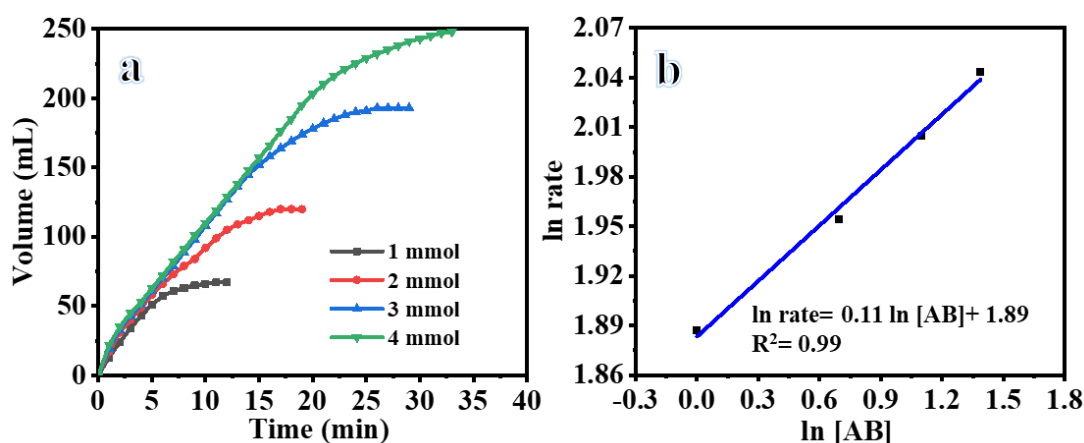

Figure 5. (**a**) Influence of AB concentration on H_2 production, and (**b**) H_2 production rate vs. AB concentration on logarithmic scale (25 mg of photocatalyst, 25 °C, and 1000 rpm).

3.4. Influence of Reaction Temperature

Figure 6a plots the H_2 production rate vs time in the presence of composite NFs at different temperatures. The figure illustrates that the photodehydrogenation of AB was observed to rise as the reaction temperature was elevated from 25 to 40 °C. This can be attributed to the enhanced mobility of charge carriers and the interfacial transfer of charges at higher temperatures. With the rise in reaction temperature, there is a corresponding rise in the mobility of photoelectron–hole pairs. This results in a more rapid combination of electrons with adsorbed oxygen and a quicker generation of OH radicals in conjunction with -OH [39–41]. Consequently, the AB photodehydrogenation process is enhanced. A linear correlation is observed between the values of K and 1/T, as depicted in Figure 6b. estimated activation energy (E_a) is 35.19 KJ mol^{-1}.
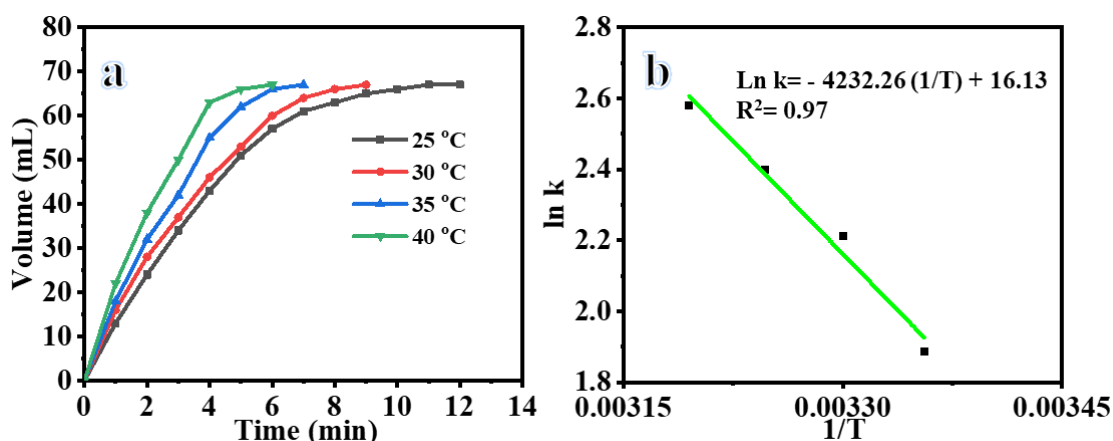

Figure 6. (**a**) Influence of reaction temperature on H_2 production, and (**b**) ln (*k*, rate constant) vs. temperature inverse (25 mg of photocatalyst, 1 mmol AB, and 1000 rpm).

3.5. Catalyst Recyclability Data

In order to investigate the extended stability and recyclability of the fabricated composite NFs, a series of photocatalytic experiments were conducted using the composite NFs over the course of five cycles (Figure 7). As depicted in Figure 7, a notable photocatalytic response was observed, accompanied by a minimal reduction in the catalytic performance. This observation shows that the newly developed photocatalytic composite NFs exhibit longevity in the catalytic reaction, and the photodegradation activity of the catalyst showed a little decrease (~10%) after five runs. The data show that the catalyst is stable and recyclable.
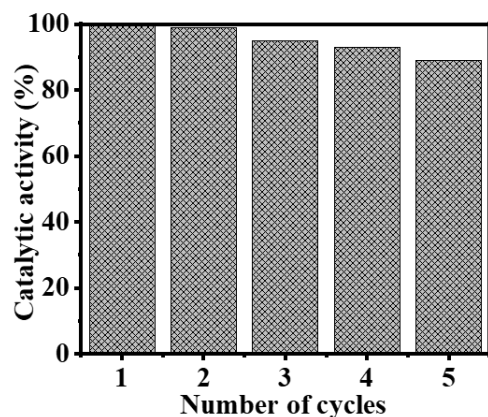

Figure 7. Catalyst recyclability data of composite NFs (25 mg of photocatalyst, 25 °C, 1 mmol AB, and 1000 rpm).

3.6. Comparison of Our Results with the Literature

The catalytic activity of the current composite NF catalyst for H_2 production was compared with others reported in the literature, as shown in Table 1. The results obtained from the photohydrolysis of AB in the presence of catalyst $NiTiO_3/TiO_2$-decorated CNFs for H_2 production were compared with the catalysts reported in the literature with titanate as an active ingredient. Chandra et al. demonstrated the photocatalytic activity of Rh/g-Al_2O_3 in the photohydrolysis of AB to produce H_2 at room temperature [42]. Their study determined the activation energy to be 21 kJ mol^{-1}. Zhu et al. synthesized Cu–ZrO_2 xerogel photocatalysts via a facile two-step approach involving an epoxide-driven sol–gel method followed by chemical reduction [43]. The 15% Cu–ZrO_2 showed the best catalytic activity with a maximum H_2 production rate of 0.384 mol$_{(H2)}$ mol$_{(cat)}^{-1}$ min^{-1}. The kinetics study revealed that the photohydrolysis of AB followed first-order kinetics when 15% Cu–ZrO_2 xerogel was used, with an activation energy of 22.34 kJ mol^{-1}. Their catalyst was stable and recyclable even after five cycles of the experiment. Chen et al. synthesized a SiO_2-encompassed Co@N-doped porous carbon catalyst. This novel recyclable catalyst was further employed for the calcination of zeolitic imidazolate framework-67@SiO_2 microtubes at high temperatures in a N_2 atmosphere [44]. The catalyst obtained from the calcination at 800 °C exhibited a high H_2 generation rate of 8.4 mol$_{(H2)}$ mol$_{(cat)}^{-1}$ min^{-1} with an activation energy of 36.1 kJ mol^{-1}. Gao et al. synthesized monodisperse Ni nanoparticles via a facile technique and then anchored them on graphitic carbon nitride (g-C_3N_4) nanosheets through a self-assembly process [37]. They determined an optimum AB photohydrolysis rate corresponding to a 3.2 nm size of Ni NPs with a TOF of 18.7 mol$_{(hydrogen)}$ mol$_{(catalyst)}^{-1}$ min^{-1} and an activation energy of 36 kJ mol^{-1}. Wang et al. employed TiO_2(B) nanotubes (NTs) that supported metal Cu/Ni nanoparticles for the catalytic hydrolysis of ammonia borane under visible light [45]. They synthesized the TiO_2 NTs via a hydrothermal technique and then loaded them with Cu/Ni metal nanoparticles via the impregnation–reduction method. The H_2 generation rate of 15.90 mol$_{(H2)}$ mol$_{(cat)}^{-1}$ min^{-1} was obtained using $Cu_{0.64}Ni_{0.36}$-TiO_2 NTs with an activation energy of 36.14 kJ mol^{-1}. In another study, Wang et al. employed TiO_2 with monoclinic-phase (TiO_2(B)) and anatase-phase composite

(TiO_2(B)/anatase) loaded with 3.66 wt.% CuNi alloy nanoparticles (NPs) as a photocatalyst for hydrogen generation from ammonia borane [19]. The as-synthesized $Cu_{0.36}Ni_{0.64}$-T700 catalysts exhibited the highest H_2 generation rate of 21.87 $mol_{(H2)}$ $mol_{(cat)}^{-1}$ min^{-1} with an activation energy of 27.40 kJ mol^{-1}. Cheng et al. employed MoO_{3-x} nanosheets to enhance the hydrogen production rate from ammonia borane under visible light [46]. They obtained a TOF of 5.74 $mol_{(H2)}$ $mol_{(cat)}^{-1}$ min^{-1}. Lu et al. immobilized Cu–Ni nanoparticles (NPs) in MCM-41 employing a liquid impregnation–reduction technique [47]. The produced composite $Cu_{0.2}Ni_{0.8}$/MCM-41 was utilized for the generation of H_2, and it performed well, yielding a TOF of 10.7 mol H_2 (mol cat)$^{-1}$ min^{-1} with an activation energy of 38 kJ mol^{-1}.

Table 1. Performance comparison of our catalyst with others reported in the literature for H_2 production from AB.

Catalyst	TOF, $mol_{(H2)}$ $mol_{(cat)}^{-1}$ min^{-1}	E_a, kJ mol^{-1}	Ref.
Rh/g-Al_2O_3	-	21	[42]
$CuZrO_2$	0.384	22.34	[43]
Co@CeN@SiO_2	8.4	36.1	[44]
Ni/g-C_3N_4	18.7	36	[37]
$Cu_{0.64}Ni_{0.36}$-TiO_2(B) NTs	15.9	36.14	[45]
$Cu_{0.36}Ni_{0.64}$-T700	21.87	27.40	[19]
MoO_3-x	5.74	--	[46]
$Cu_{0.2}Ni_{0.8}$/MCM-41	10.7	38	[47]
$NiTiO_3$/TiO_2@CNFs	22.02	35.19	This Work

3.7. Photodehydrogenation Mechanism

It has been hypothesized that the composite NFs would undergo the photohydrolysis process of AB photodehydrogenation. The process of separating electron (e^-)–hole (h^+) pairs produced by visible illumination in the composite NFs can be understood by evaluating the conduction band (CB) and valence band (VB) potentials of the constituent materials. The energies in controversy were computed utilizing the subsequent empirical formulas [48]:

$$E_{CB} = \chi - E_e - 0.5E_g \tag{1}$$

$$E_{VB} = E_{CB} + E_g \tag{2}$$

Equation (1) represents the relationship between the conduction band energy (E_{CB}), the electron energy (E_e), and the bandgap energy (E_g) in the context of the E_{CB}. Equation (2) represents the relationship between the valence band energy (E_{VB}) and E_{CB}, taking into account the bandgap energy. Furthermore, the energy of liberated electrons in relation to the Normal Hydrogen Electrode (NHE) is denoted as Ee and measures 4.5 electron volts [48]. The bandgap energy of the semiconductor is denoted by "Eg". The symbol χ is utilized to represent the electronegativity of the semiconductor. According to a study, the potentials of CB and VB of ilmenite nickel titanite in comparison to SHE were determined to be +0.20 eV and +2.38 eV, respectively. Ilmenite nickel titanite exhibits a lower bandgap of 2.62 eV in comparison to pristine TiO_2, which has a bandgap of 3.2 eV. As a result, the VB position of ilmenite nickel titanite is higher at +2.38 eV in contrast to TiO_2, which is at +2.94 eV. This higher VB position of ilmenite nickel titanite facilitates the transfer of h^+ from its VB to the VB of TiO_2. Upon photoexcitation, the photogenerated h^+ undergoes a reaction with H_2O/OH^-, resulting in the production of OH radicals [39]. It is noteworthy that the CB of ilmenite nickel titanite is situated at a lower energy level than that of TiO_2 (-0.29 eV). Upon exposure to light, the VB e^- in ilmenite nickel titanite undergo excitation and transition to the CB, leading to the partial vacancy of the VB. Consequently, e^- from

the CB of TiO_2 are transferred to the CB of ilmenite nickel titanite. Its involvement in the photodehydrogenation process implies its potential as a proficient sensitizer that can effectively harness visible illumination. The mobility of photogenerated e^- in ilmenite nickel titanite is observed to be directed towards the surface of the CNFs, indicating a high degree of separation efficiency between photogenerated e and h^+ with low rates of recombination [40]. The O_2 molecules undergo a reaction with the photogenerated electron located in the conduction band of ilmenite nickel titanite, resulting in the production of $\bullet O_2^-$ without any recombination with the holes that are present on the surface of TiO_2 [37]. The resulting oxide anions ($\bullet O_2^-$) undergo a reaction with hydrogen ions, leading to the formation of hydroperoxyl radicals (HOO$\bullet$), which subsequently induce modifications to the AB molecule present in the solution. According to a study, it was found that the composite NFs exhibited a greater level of photocatalytic activity compared to that of the pristine TiO_2. The mechanism of photodehydrogenation of AB utilizing composite NFs can be demonstrated as presented in Figure 8 [13,15,37,41,49].
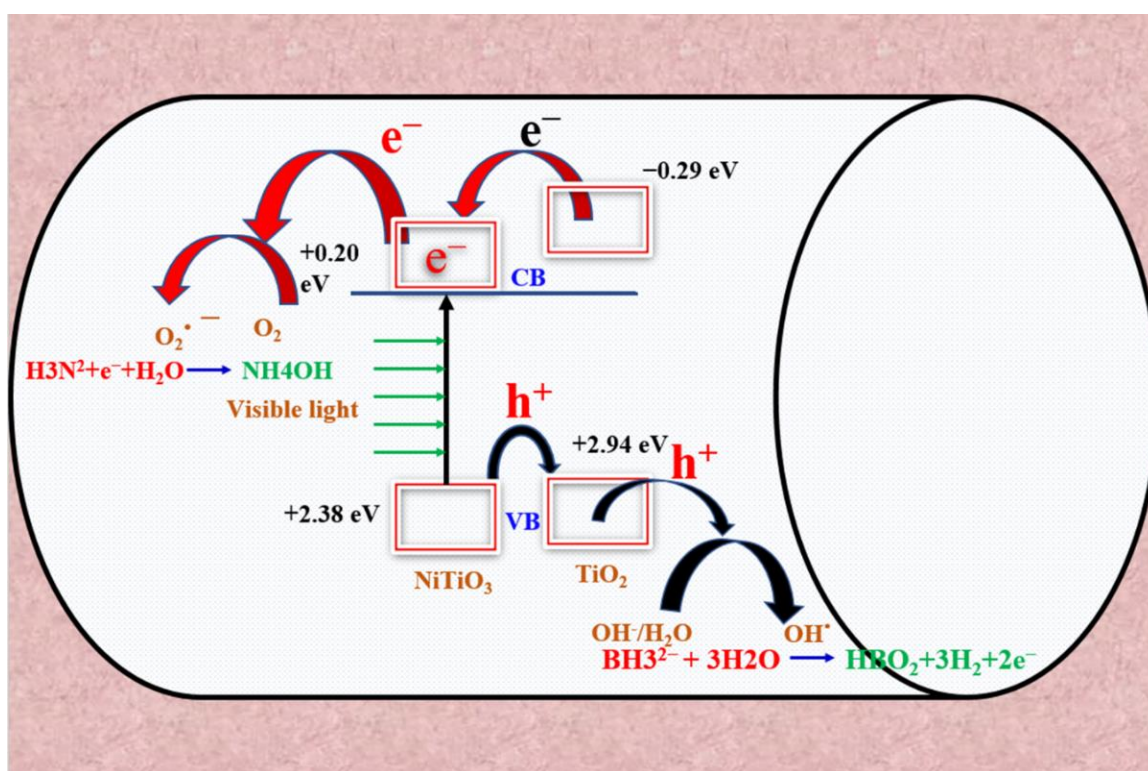

Figure 8. Schematic representation of the photodehydrogenation of AB.

4. Conclusions

In this study, photocatalytic composite NFs consisting of $NiTiO_3/TiO_2$@CNFS were synthesized through the electrospinning technique and used for H_2 generation from AB. The use of photocatalytic composite NFs in the photohydrolysis process resulted in a significant increase in the catalytic efficiency and a substantial production of H_2 compared to pristine TiO_2. Furthermore, the photocatalytic composite NFs exhibited remarkable photocatalytic performance, as indicated by the estimated low activation energy (35.19 kJ mol^{-1}). The experimental findings show that the photocatalytic composite NFs with a loading of 25 mg had a good catalytic performance for H_2 generation, producing stoichiometric H_2 in 11 min using 1 mmol AB under visible light at 25 °C and 1000 rpm. An increase in catalyst loading to 50, 75, and 100 mg led to a corresponding reduction in the reaction time to 7, 5, and 4 min, respectively. The findings from the kinetics investigations suggest that the rate of the photohydrolysis reaction is directly proportional to the amount of catalyst in the reaction system, adhering to a first-order reaction rate. Furthermore, it was observed

that the reaction rate remains unaffected by the concentration of AB, thereby suggesting a reaction of zero order. Increasing the reaction temperature results in a decrease in the duration of the photohydrolysis reaction. The composite nanofibers demonstrated remarkable and consistent effectiveness throughout five consecutive cycles. The results suggest that composite NFs possess the capacity to function as a feasible substitute for costly catalysts in the process of H_2 generation from AB. The photocatalytic composite NFs demonstrated a consistent and enduring production of H_2 throughout reusability and stability assessments for five cycles. This suggests that they have the potential to serve as viable photocatalysts for practical uses.

Author Contributions: Conceptualization, A.A. and A.Y.; methodology, A.Y. and I.Y.Q.; validation, M.M.E.-H. and S.M.M.; formal analysis, I.M.M. and I.Y.Q; investigation, N.Z. and S.M.M.; resources, A.A. and A.S.M.A.; data curation, M.M.E.-H. and I.M.M.; writing—original draft preparation, A.A., I.M.M. and M.M.E.-H.; writing—review and editing, A.Y., S.M.M., I.Y.Q. and A.S.M.A.; visualization, N.Z. and A.S.M.A.; supervision, A.A., I.M.M., N.Z., A.Y. and M.M.E.-H.; project administration, S.M.M., I.Y.Q. and A.S.M.A.; funding acquisition, N.Z. All authors have read and agreed to the published version of the manuscript.

Institutional Review Board Statement: Not applicable.

Data Availability Statement: Not applicable.

Conflicts of Interest: The authors declare no conflict of interest.

References

1. He, W.; Abbas, Q.; Alharthi, M.; Mohsin, M.; Hanif, I.; Vinh Vo, X.; Taghizadeh-Hesary, F. Integration of Renewable Hydrogen in Light-Duty Vehicle: Nexus between Energy Security and Low Carbon Emission Resources. *Int. J. Hydrog. Energy* **2020**, *45*, 27958–27968. [CrossRef]
2. Omer, A.M. Green Energies and the Environment. *Renew. Sustain. Energy Rev.* **2008**, *12*, 1789–1821. [CrossRef]
3. Zhang, S.; Xu, J.; Cheng, H.; Zang, C.; Bian, F.; Sun, B.; Shen, Y.; Jiang, H. Photocatalytic H_2 Evolution from Ammonia Borane: Improvement of Charge Separation and Directional Charge Transmission. *ChemSusChem* **2020**, *13*, 5264–5272. [CrossRef]
4. Aziz, M. Liquid Hydrogen: A Review on Liquefaction, Storage, Transportation, and Safety. *Energies* **2021**, *14*, 5917. [CrossRef]
5. Van Hoecke, L.; Laffineur, L.; Campe, R.; Perreault, P.; Verbruggen, S.W.; Lenaerts, S. Challenges in the Use of Hydrogen for Maritime Applications. *Energy Env. Sci.* **2021**, *14*, 815–843. [CrossRef]
6. Dematteis, E.M.; Barale, J.; Corno, M.; Sciullo, A.; Baricco, M.; Rizzi, P. Solid-State Hydrogen Storage Systems and the Relevance of a Gender Perspective. *Energies* **2021**, *14*, 6158. [CrossRef]
7. Ahmad, M.A.N.; Sazelee, N.; Ali, N.A.; Ismail, M. An Overview of the Recent Advances of Additive-Improved $Mg(BH_4)_2$ for Solid-State Hydrogen Storage Material. *Energies* **2022**, *15*, 862. [CrossRef]
8. Zhang, G.; Morrison, D.; Bao, G.; Yu, H.; Yoon, C.W.; Song, T.; Lee, J.; Ung, A.T.; Huang, Z. An Amine–Borane System Featuring Room-Temperature Dehydrogenation and Regeneration. *Angew. Chem. Int. Ed.* **2021**, *60*, 11725–11729. [CrossRef]
9. Mboyi, C.D.; Poinsot, D.; Roger, J.; Fajerwerg, K.; Kahn, M.L.; Hierso, J. The Hydrogen-Storage Challenge: Nanoparticles for Metal-Catalyzed Ammonia Borane Dehydrogenation. *Small* **2021**, *17*, 2102759. [CrossRef]
10. Giri, S.; Tripathi, A.K. Hydrogen Utilisation via Ammonia Borane Dehydrogenation and Regeneration: A Review. In *Advances in Chemical, Bio and Environmental Engineering*; Ratan, J.K., Sahu, D., Pandhare, N.N., Bhavanam, A., Eds.; Springer: Berlin/Heidelberg, Germany, 2022; pp. 651–669.
11. Liu, M.; Zhou, L.; Luo, X.; Wan, C.; Xu, L. Recent Advances in Noble Metal Catalysts for Hydrogen Production from Ammonia Borane. *Catalysts* **2020**, *10*, 788. [CrossRef]
12. Li, H.; Yan, Y.; Feng, S.; Zhu, Y.; Chen, Y.; Fan, H.; Zhang, L.; Yang, Z. Transition Metal Tuned Semiconductor Photocatalyst CuCo/β-SiC Catalyze Hydrolysis of Ammonia Borane to Hydrogen Evolution. *Int. J. Hydrog. Energy* **2019**, *44*, 8307–8314. [CrossRef]

13. Yousef, A.; Barakat, N.A.M.; Khalil, K.A.; Unnithan, A.R.; Panthi, G.; Pant, B.; Kim, H.Y. Photocatalytic Release of Hydrogen from Ammonia Borane-Complex Using Ni(0)-Doped TiO2/C Electrospun Nanofibers. *Colloids Surf. A Physicochem. Eng. Asp.* **2012**, *410*, 59–65. [CrossRef]

14. Wang, C.; Zhao, J.; Du, X.; Sun, S.; Yu, X.; Zhang, X.; Lu, Z.; Li, L.; Yang, X. Hydrogen Production from Ammonia Borane Hydrolysis Catalyzed by Non-Noble Metal-Based Materials: A Review. *J. Mater. Sci.* **2021**, *56*, 2856–2878. [CrossRef]

15. Wei, L.; Yang, Y.; Yu, Y.-N.; Wang, X.; Liu, H.; Lu, Y.; Ma, M.; Chen, Y. Visible-Light-Enhanced Catalytic Hydrolysis of Ammonia Borane Using RuP2 Quantum Dots Supported by Graphitic Carbon Nitride. *Int. J. Hydrog. Energy* **2021**, *46*, 3811–3820. [CrossRef]

16. Wei, L.; Zhang, Y.; Liu, J.; Li, Y.; Lu, Y.; Liu, H. Visible-Light-Enhanced Hydrogen Evolution from Catalytic Hydrolysis of Ammonia Borane Using Ru Nanoparticles Supported on CdS-Modified Graphitic Carbon Nitride. *New. J. Chem.* **2022**, *46*, 19731–19739. [CrossRef]

17. Simagina, V.I.; Komova, O.V.; Ozerova, A.M.; Netskina, O.V.; Odegova, G.V.; Kayl, N.L.; Filippov, T.N. TiO$_2$-Based Photocatalysts for Controllable Hydrogen Evolution from Ammonia Borane. *Catal. Today* **2021**, *379*, 149–158. [CrossRef]

18. Yan, Y.; Zhang, C.; Jia, T.; Li, H.; Shen, K. Efficient Hydrogen Production by an RGO/TiO$_2$ Composite Material from Ammonia Borane Hydrolysis in a Photocatalytic Reactor. *Energy Fuels* **2021**, *35*, 16065–16074. [CrossRef]

19. Wang, C.; Yu, X.; Zhang, X.; Lu, Z.; Wang, X.; Han, X.; Zhao, J.; Li, L.; Yang, X. Enhanced Hydrogen Production from Ammonia Borane over CuNi Alloy Nanoparticles Supported on TiO2(B)/Anatase Mixed-Phase Nanofibers with High Specific Surface Area. *J. Alloys Compd.* **2020**, *815*, 152431. [CrossRef]

20. Asim, M.; Zhang, S.; Ai, M.; Maryam, B.; Wang, Y.; Li, X.; Yang, J.; Zou, J.-J.; Pan, L. Photohydrolysis of Ammonia Borane for Effective H$_2$ Evolution via Hot Electron-Assisted Energy Cascade of Au-WO$_{2.72}$/TiO$_2$. *Ind. Eng. Chem. Res.* **2022**, *61*, 11429–11435. [CrossRef]

21. Yan, Y.; Li, J.; Jia, T.; Li, H.; Shen, K.; He, Z. Preparation of TiO$_2$-Based Photocatalysts Synergistically Modified with Fe^{3+}–Graphene and Their Visible-Light-Catalyzed Hydrogen Production from Ammonia Borane. *Energy Fuels* **2021**, *35*, 16035–16045. [CrossRef]

22. Wang, Y.; Shen, G.; Zhang, Y.; Pan, L.; Zhang, X.; Zou, J.-J. Visible-Light-Induced Unbalanced Charge on NiCoP/TiO$_2$ Sensitized System for Rapid H$_2$ Generation from Hydrolysis of Ammonia Borane. *Appl. Catal. B* **2020**, *260*, 118183. [CrossRef]

23. Trang, N.T.T.; Khang, D.M.; Dung, D.D.; Trung, N.N.; Phuong, N.T.; Bac, L.H. Synthesis of Ilmenite NiTiO3 Rods and Effect of PH on Rhodamine B Textile Dye Degradation under LED Visible-Light Irradiation. *J. Electron. Mater.* **2021**, *50*, 7188–7197. [CrossRef]

24. Van, K.H.; Ramacharyulu, P.V.R.K.; Youn, D.H.; Kim, C.W. Determining Anisotropic Reactive Facet of Ilmenite Photocatalyst with Hubbard U Assisted Density Functional Theory. *Comput. Mater. Sci.* **2023**, *219*, 112024. [CrossRef]

25. Pham, T.-T.; Shin, E.W. Inhibition of Charge Recombination of NiTiO3 Photocatalyst by the Combination of Mo-Doped Impurity State and Z-Scheme Charge Transfer. *Appl. Surf. Sci.* **2020**, *501*, 143992. [CrossRef]

26. Jiang, K.; Jung, H.; Pham, T.-T.; Dao, D.Q.; Nguyen, T.K.A.; Yu, H.; Men, Y.; Shin, E.W. Modification of NiTiO3 Visible Light-Driven Photocatalysts by Nb Doping and NbOx Heterojunction: Oxygen Vacancy in the Nb-Doped NiTiO3 Structure. *J. Alloys Compd.* **2021**, *861*, 158636. [CrossRef]

27. Li, S.; Hu, S.; Jiang, W.; Liu, Y.; Zhou, Y.; Liu, Y.; Mo, L. Hierarchical Architectures of Bismuth Molybdate Nanosheets onto Nickel Titanate Nanofibers: Facile Synthesis and Efficient Photocatalytic Removal of Tetracycline Hydrochloride. *J. Colloid Interface Sci.* **2018**, *521*, 42–49. [CrossRef]

28. Huang, J.; Jiang, Y.; Li, G.; Xue, C.; Guo, W. Hetero-Structural NiTiO$_3$/TiO$_2$ Nanotubes for Efficient Photocatalytic Hydrogen Generation. *Renew. Energy* **2017**, *111*, 410–415. [CrossRef]

29. Komaraiah, D.; Radha, E.; Sivakumar, J.; Ramana Reddy, M.V.; Sayanna, R. Photoluminescence and Photocatalytic Activity of Spin Coated Ag+ Doped Anatase TiO$_2$ Thin Films. *Opt. Mater.* **2020**, *108*, 110401. [CrossRef]

30. Panthi, G.; Barakat, N.A.M.; Abdelrazek Khalil, K.; Yousef, A.; Jeon, K.-S.; Kim, H.Y. Encapsulation of CoS Nanoparticles in PAN Electrospun Nanofibers: Effective and Reusable Catalyst for Ammonia Borane Hydrolysis and Dyes Photodegradation. *Ceram. Int.* **2013**, *39*, 1469–1476. [CrossRef]

31. Yousef, A.; Barakat, N.A.M.; Amna, T.; Al-Deyab, S.S.; Hassan, M.S.; Abdel-hay, A.; Kim, H.Y. Inactivation of Pathogenic Klebsiella Pneumoniae by CuO/TiO2 Nanofibers: A Multifunctional Nanomaterial via One-Step Electrospinning. *Ceram. Int.* **2012**, *38*, 4525–4532. [CrossRef]

32. Yousef, A.; Barakat, N.A.M.; Kim, H.Y. Electrospun Cu-Doped Titania Nanofibers for Photocatalytic Hydrolysis of Ammonia Borane. *Appl. Catal. A Gen.* **2013**, *467*, 98–106. [CrossRef]

33. Yousef, A.; Brooks, R.M.; El-Halwany, M.M.; EL-Newehy, M.H.; Al-Deyab, S.S.; Barakat, N.A.M. Cu 0/S-Doped TiO$_2$ Nanoparticles-Decorated Carbon Nanofibers as Novel and Efficient Photocatalyst for Hydrogen Generation from Ammonia Borane. *Ceram. Int.* **2016**, *42*, 1507–1512. [CrossRef]

34. Yousef, A.; Brooks, R.M.; El-Halwany, M.M.; Obaid, M.; El-Newehy, M.H.; Al-Deyab, S.S.; Barakat, N.A.M. A Novel and Chemical Stable Co–B Nanoflakes-like Structure Supported over Titanium Dioxide Nanofibers Used as Catalyst for Hydrogen Generation from Ammonia Borane Complex. *Int. J. Hydrog. Energy* **2016**, *41*, 285–293. [CrossRef]

35. Yousef, A.; El-Halwany, M.M.; Barakat, N.A.M.; Al-Maghrabi, M.N.; Kim, H.Y. Cu0- Doped TiO$_2$ Nanofibers as Potential Photocatalyst and Antimicrobial Agent. *J. Ind. Eng. Chem.* **2015**, *26*, 251–258. [CrossRef]

36. Maafa, I.M.; Ali, M.A. Enhanced Organic Pollutant Removal Efficiency of Electrospun NiTiO$_3$/TiO$_2$-Decorated Carbon Nanofibers. *Polymers* **2023**, *15*, 109–125. [CrossRef]

37. Gao, M.; Yu, Y.; Yang, W.; Li, J.; Xu, S.; Feng, M.; Li, H. Ni Nanoparticles Supported on Graphitic Carbon Nitride as Visible Light Catalysts for Hydrolytic Dehydrogenation of Ammonia Borane. *Nanoscale* **2019**, *11*, 3506–3513. [CrossRef]

38. Metin, Ö.; Mazumder, V.; Özkar, S.; Sun, S. Monodisperse Nickel Nanoparticles and Their Catalysis in Hydrolytic Dehydrogenation of Ammonia Borane. *J. Am. Chem. Soc.* **2010**, *132*, 1468–1469. [CrossRef]

39. Moradi, M.; Vasseghian, Y.; Khataee, A.; Harati, M.; Arfaeinia, H. Ultrasound-assisted Synthesis of FeTiO$_3$/GO Nanocomposite for Photocatalytic Degradation of Phenol under Visible Light Irradiation. *Sep. Purif. Technol.* **2021**, *261*, 118274. [CrossRef]

40. Zhang, M.; Shao, C.; Mu, J.; Huang, X.; Zhang, Z.; Guo, Z.; Zhang, P.; Liu, Y. Hierarchical Heterostructures of Bi$_2$MoO$_6$ on Carbon Nanofibers: Controllable Solvothermal Fabrication and Enhanced Visible Photocatalytic Properties. *J. Mater. Chem.* **2012**, *22*, 577–584. [CrossRef]

41. Song, J.; Wu, F.; Lu, Y.; Zhang, X.; Li, Z. CeVO$_4$/CeO$_2$ Heterostructure-Supported Co Nanoparticles for Photocatalytic H$_2$ Production from Ammonia Borane under Visible Light. *ACS Appl. Nano Mater.* **2021**, *4*, 4800–4809. [CrossRef]

42. Chandra, M.; Xu, Q. Room temperature hydrogen generation from aqueous ammonia-borane using noble metal nano-clusters as highly active catalysts. *J. Power Sources* **2007**, *168*, 135–142. [CrossRef]

43. Zhu, J.; Ma, L.; Feng, J.; Geng, T.; Wei, W.; Xie, J. Facile synthesis of Cu nanoparticles on different morphology ZrO$_2$ supports for catalytic hydrogen generation from ammonia borane. *J. Mater. Sci. Mater. Electron.* **2018**, *29*, 14971–14980. [CrossRef]

44. Chen, M.; Xiong, R.; Cui, X.; Wang, Q.; Liu, X. SiO$_2$-Encompassed Co@N-Doped Porous Carbon Assemblies as Recyclable Catalysts for Efficient Hydrolysis of Ammonia Borane. *Langmuir* **2019**, *35*, 671–677. [CrossRef]

45. Wang, C.; Sun, D.; Yu, X.; Zhang, X.; Lu, Z.; Wang, X.; Zhao, J.; Li, L.; Yang, X. Cu/Ni nanoparticles supported on TiO$_2$(B)nanotubes as hydrogen generation photocatalysts via hydrolysis of ammonia borane. *Inorg. Chem. Front.* **2018**, *5*, 2038–2044. [CrossRef]

46. Cheng, H.; Kamegawa, T.; Mori, K.; Yamashita, H. Surfactant-free nonaqueous synthesis of plasmonic molybdenum oxide nanosheets with enhanced catalytic activity for hydrogen generation from ammonia borane under visible light. *Angew Chem. Int.* **2014**, *53*, 2910–2914. [CrossRef]

47. Lu, Z.-H.; Li, J.; Feng, G.; Yao, Q.; Zhang, F.; Zhou, R.; Tao, D.; Chen, X.; Yu, Z. Synergistic catalysis of MCM-41 immobilized Cu-Ni nanoparticles in hydrolytic dehydrogeneration of ammonia borane. *Int. J. Hydrogen Energy* **2014**, *39*, 13389–13395. [CrossRef]

48. Xu, Y.; Schoonen, M.A.A. The Absolute Energy Positions of Conduction and Valence Bands of Selected Semiconducting Minerals. *Am. Mineral.* **2000**, *85*, 543–556. [CrossRef]

49. Wen, M.; Kuwahara, Y.; Mori, K.; Zhang, D.; Li, H.; Yamashita, H. Synthesis of Ce Ions Doped Metal–Organic Framework for Promoting Catalytic H$_2$ Production from Ammonia Borane under Visible Light Irradiation. *J. Mater. Chem. A Mater.* **2015**, *3*, 14134–14141. [CrossRef]